

# Comparing SAM 2 and SAM 3 for Zero-Shot Segmentation of 3D Medical Data

Satrajit Chakrabarty <sup>1,2</sup> and Ravi Soni<sup>1</sup>

<sup>1</sup>GE HealthCare, San Ramon, CA, USA

<sup>2</sup>Corresponding author: [satrajit.chakrabarty@gehealthcare.com](mailto:satrajit.chakrabarty@gehealthcare.com)

**Abstract.** Foundation models for promptable segmentation, including SAM, SAM 2, and the recently released SAM 3, have renewed interest in zero-shot segmentation of medical imaging. Although these models perform strongly on natural images, their behavior on medical data remains insufficiently characterized. While SAM 2 is widely used for annotation in 3D medical workflows, SAM 3 introduces a new perception backbone, detector-tracker pipeline, and concept-level prompting that may alter its behavior under spatial prompts. We present the first controlled comparison of SAM 2 and SAM 3 for zero-shot segmentation of 3D medical volumes and videos under purely visual prompting, with concept mechanisms disabled. We assess whether SAM 3 can serve as an out-of-the-box replacement for SAM 2 without customization. We benchmark both models on 16 public datasets (CT, MRI, 3D and cine ultrasound, endoscopy) covering 54 anatomical structures, pathologies, and surgical instruments. Prompts are restricted to the first frame and use four modes: single-click, multi-click, bounding box, and dense mask. This design standardizes preprocessing, prompt placement, propagation rules, and metric computation to disentangle prompt interpretation from propagation. Prompt-frame analysis shows that SAM 3 provides substantially stronger initialization than SAM 2 for click prompting across most structures. In full-volume analysis, SAM 3 retains this advantage for complex, vascular, and soft-tissue anatomies, emerging as the more versatile general-purpose segmenter. While SAM 2 remains competitive for compact, rigid organs under strong spatial guidance, it frequently fails on challenging targets where SAM 3 succeeds. Overall, our results suggest that SAM 3 is the superior default choice for most medical segmentation tasks, particularly those involving sparse user interaction or complex anatomical topology.

**Keywords:** Foundation models · Promptable segmentation · Zero-shot segmentation · SAM · SAM 2 · SAM 3 · CT · MRI · Ultrasound.

## 1 Introduction

Foundation models for promptable segmentation have reshaped interactive medical image analysis. The Segment Anything Model (SAM) [1] introduced a general-purpose framework for zero-shot segmentation of 2D images using point, box, and mask prompts. SAM 2 [2] extended this approach to videos and 3D-like sequences by adding a memory-based transformer architecture for frame-to-frame propagation, thus significantly improving spatio-temporal consistency. The most recent iteration of SAM, namely SAM 3 [3], introduced a unified Perception Encoder backbone shared by an image-level detector and a video tracker, adopting a DETection TRansformer (DETR)-style architecture [4], a decoupled presence token for recognition, and a redesigned fusion and mask-prediction stack. These changes were engineered to support Promptable Concept Segmentation and large-scale open-vocabulary training, but they also modify the model’s visual-prompt behavior relative to SAM 2.

Although these models exhibit strong performance on natural images, their behavior on medical imaging remains inadequately characterized. Medical data impose unique challenges, including modality-specific contrast characteristics, low signal-to-noise ratios, and substantial variation across depth or time. Over the past year, SAM 2 has become a widely used baseline for zero-shot segmentation of 3D medical data because its memory module provides stable slice-to-slice propagation. Prior studies have performed comparative analyses of SAM and SAM 2 using various

---

\*This manuscript reports results from early experiments of a larger ongoing study. Subsequent analyses may lead to refinements or extensions of the findings presented here.

prompting modes on medical data [5,6,7]. These evaluations effectively served as backwards compatibility checks, assessing how newer releases in the SAM family behave under standardized prompting conditions on medical data. In a similar spirit, with the introduction of SAM 3’s new detector–tracker pipeline, presence-based recognition, and substantially different mask heads, the question arises whether SAM 3 maintains or improves the spatial and propagation behavior that previously made SAM 2 a suitable starting point for 3D medical segmentation. A central motivation of this work is, therefore, to determine whether SAM 3 can function as an out-of-the-box drop-in replacement for SAM 2 in 3D medical data annotation workflows, without concept prompts, fine-tuning, or task-specific adaptations.

To answer this question, we conducted a large-scale, controlled comparison of SAM 2 and SAM 3 across 16 publicly available datasets spanning CT, MRI, ultrasound, and endoscopy modalities, covering 54 anatomical structures, pathologies, and surgical instruments. Our evaluation standardized preprocessing, prompt placement, propagation rules, and metric computation across modalities. We benchmarked four prompting strategies namely single-click, multi-click, bounding box, and mask prompts, each applied only to the first frame, ensuring a consistent and interpretable comparison of initialization and propagation behavior.

This study makes three main contributions:

- A unified, cross-modality evaluation framework for comparing SAM 2 and SAM 3 under identical visual prompts, with all concept-level mechanisms in SAM 3 disabled.
- A comprehensive empirical analysis of prompt-frame as well as full-volume/sequence performance across 16 datasets, revealing a structural divergence in performance: while SAM 3 dominates initialization and tracking of complex topologies, SAM 2 retains specific advantages for some compact, rigid anatomy.
- A practical assessment of model interchangeability, providing the first systematic evidence on whether SAM 3 can serve as a drop-in replacement for SAM 2 in real-world 3D medical annotation workflows.

By isolating visual-prompt behavior and conducting extensive cross-modality experiments, this work clarifies the complementary strengths of SAM 2 and SAM 3 and provides guidance for selecting between these models in clinical and research settings.

## 2 Methods

### 2.1 Comparison rationale

The objective of this study is to compare SAM 2 and SAM 3 under controlled and identical prompting conditions for medical image segmentation in 3D volumes and medical video sequences. SAM 3 contains components designed for Promptable Concept Segmentation, such as the presence head and text–exemplar fusion modules. All concept-based mechanisms are disabled in our evaluation so that both models operate strictly within the visual prompting regime. This configuration creates a direct comparison between the two architectures and isolates the effects of visual prompt encoding and propagation without the influence of text, concept embeddings, or exemplar-based recognition.

### 2.2 Model Overview

SAM 2 [2] is an encoder–decoder architecture built upon the Hiera (Hierarchical Vision Transformer) backbone [8]. Its defining feature is a streaming memory mechanism designed for semi-supervised video object segmentation. Unlike static segmenters, SAM 2 maintains a memory bank of past frame features and predictions. During inference, a memory attention module aggregates these historical features to enforce spatio-temporal consistency, allowing the model to propagate an initial mask across a 3D medical volume or video sequence.

On the other hand, SAM 3 [3] represents a shift toward a unified vision–language architecture. It replaces the separate image and memory encoders with a single Perception Encoder that jointly processes visual and textual inputs. The tracking and detection heads follow the DETR architecture [4], utilizing learnable object queries to localize targets. While SAM 3 introduces a "presence token" for semantic recognition, we disable this head for our evaluation. We utilize the SAM 3 tracker, which retains the functional logic of frame-to-frame propagation but implements it through the updated DETR-style query mechanism rather than the memory bank used in SAM 2.

### 2.3 Prompting Strategy

We evaluate three prompting strategies that represent the standard modes of operation for the SAM family of models.

**Click prompting (1+0 and 1+2).** We evaluate two click-based prompting modes: a single positive click (1,0) and a mixed positive-negative configuration (1,2). The positive click was placed near the centroid of the target structure. The negative clicks were selected from a dilated region around the target structure, ensuring that the first negative click was maximally distant from the positive click at the centroid, with subsequent negative clicks spaced apart from each other.

**Bounding-box prompting.** A tight bounding box is constructed around the ground-truth structure in the first frame. The box coordinates are processed by the prompt encoder and provide coarse geometric context for the localization of the target region.

**Mask prompting.** A binary mask from the first ground-truth frame where the corresponding structure appears, is supplied as the initial prompt. This configuration removes ambiguity regarding the initial spatial support and directly evaluates the propagation behavior of each model.

All prompts are provided only on the first frame. After this initialization, the models receive no additional interactions and proceed entirely through their respective propagation mechanisms. Both models perform frame-to-frame propagation sequentially from the first frame to the last frame of the volume without any forward-backward merging, smoothing, or post-processing.

### 2.4 Datasets

We evaluate SAM 2 and SAM 3 on sixteen publicly available medical imaging datasets spanning four imaging modalities: 3D CT, 3D MRI, ultrasound (2D cine and 3D volumes), and endoscopy video (Table 1, Figure 1). Our data selection covers a broad spectrum of anatomical structures,

Table 1: Descriptions of the medical imaging datasets used for evaluation.

Dataset Name	Modality	Description
AMOS22 [9]	CT	Abdominal organs
BTCV [10]	CT	Abdominal organs
FLARE22 [11]	CT	Abdominal organs
MSD Task06 Lung [12,13]	CT	Lung tumor segmentation
MSD Task07 Pancreas [12,13]	CT	Pancreas and pancreatic tumor
MSD Task09 Spleen [12,13]	CT	Spleen
MSD Task10 Colon [12,13]	CT	Colon cancer
TotalSegmentator [14]	CT	Abdominal organs
ACDC [15]	MRI	Cardiac chambers and myocardium
AMOS22 [9]	MRI	Abdominal organs
MSD Task02 Heart [12,13]	MRI	Left atrium
MSD Task04 Hippocampus [12,13]	MRI	Hippocampal subregions
TotalSegmentator [16]	MRI	Abdominal organs
CAMUS [17]	US (video)	Cardiac chambers
SegThy [18]	US (3D)	Thyroid, carotid arteries, jugular veins
CholecSeg8K [19,20]	Endoscopy	Cholecystectomy structures and instruments

pathological conditions, and clinical instruments across modalities, ensuring that the evaluation reflects the diversity encountered in real-world clinical imaging workflows. The CT cohorts include multi-organ abdominal benchmarks (AMOS22 [9], BTCV [10], FLARE22 [11], and TotalSegmentator [14]) together with oncologic and thoracic tasks from the MSD collection (lung tumors, pancreas and pancreatic tumors, spleen, and colon cancer) [12,13]. The MRI cohorts cover abdominal organs, cardiac structures, and neuroanatomy via AMOS22 [9], ACDC [15], MSD Task02 Heart [12,13], MSD Task04 Hippocampus [12,13], and the MRI subset of TotalSegmentator [16]. Ultrasound is represented by cardiac cine sequences from CAMUS [17] and 3D thyroid ultrasound from SegThy [18], while CholecSeg8K [19,20] provides endoscopy video frames with organ and instrument labels. All datasets were converted into a unified slice-based format to enable consistent evaluation across models and modalities. For CT datasets, images were first windowed using clinically standard ranges (e.g., soft-tissue windowing with level-width of 40/400 for abdominal CT

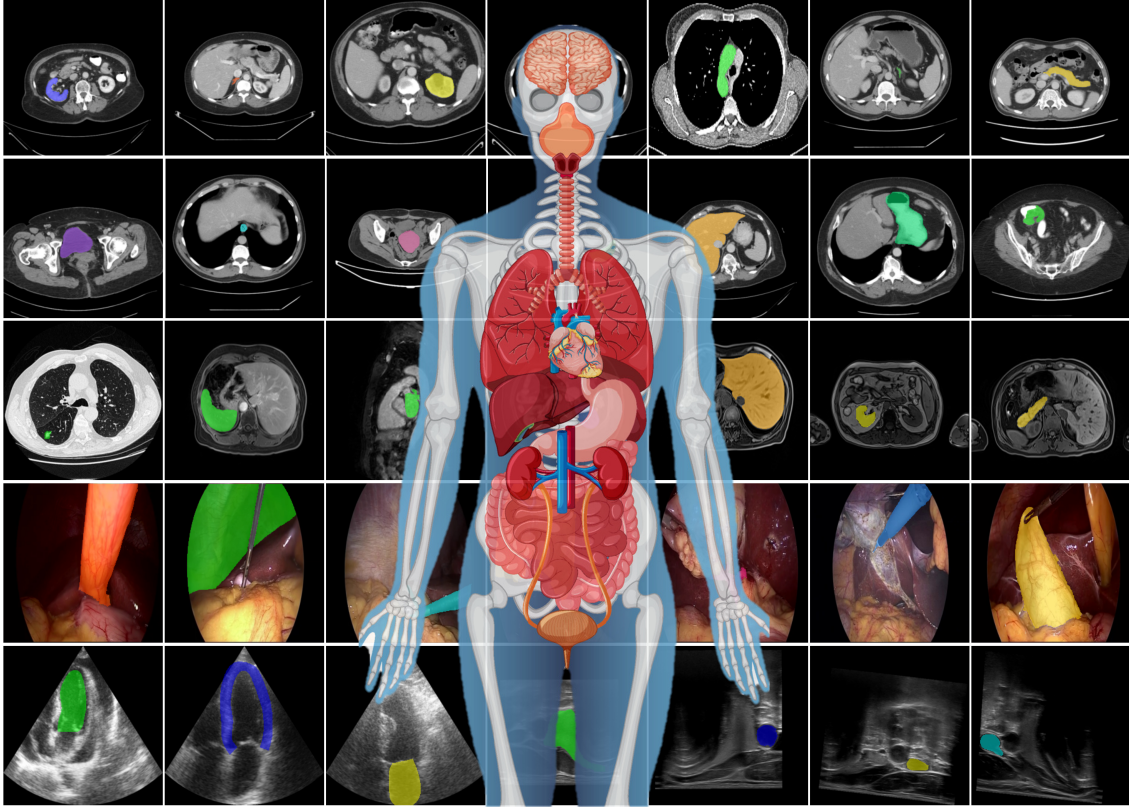


Fig. 1: Examples of images overlaid with ground-truth annotation masks from the sixteen publicly available medical imaging datasets used for evaluation in this study, spanning 3D CT, 3D MRI, ultrasound (2D cine and 3D volumes), and endoscopy. The panel layout is designed to capture variability in anatomical regions, pathologies, imaging contrast, and acquisition settings (refer to Table 1 for dataset details). The human anatomy illustration is adapted from a graphic obtained from Vecteezy.com.

and lung windowing of  $-600/1500$  for thoracic CT) before clipping and rescaling to  $[0, 255]$ . MRI volumes were normalized by extracting the intensity values between the 0.5th and 99.5th percentiles within each volume and linearly rescaling this clipped range to  $[0, 255]$ , ensuring robustness to modality-specific dynamic range differences. Ultrasound images were min-max normalized per sequence and similarly rescaled to  $[0, 255]$ . Endoscopy datasets provided color-coded semantic masks, which were converted into per-class binary masks via RGB-to-class lookup. No smoothing, interpolation, or artifact removal was applied. This standardized preprocessing ensures that SAM 2 and SAM 3 operate on identically prepared inputs across all imaging modalities.

## 2.5 Implementation Details and Evaluation Metrics

All experiments use publicly released checkpoints without any fine-tuning. For SAM 2, we use the SAM 2.1 Hiera-B+ checkpoint. The SAM 3 release does not specify multiple model variants in the paper, and we therefore adopt the standard configuration provided by the authors. Segmentation accuracy is measured using the Dice similarity coefficient (DSC). Statistical significance is assessed using paired Wilcoxon signed-rank tests on video/volume-level DSC, with significance defined at  $\alpha = 0.05$ . All evaluations were performed on NVIDIA H100 GPUs.

## 3 Results

### 3.1 Prompt-Frame Accuracy

To isolate the effect of *prompt interpretation*, defined here as the model’s ability to accurately resolve the spatial extent of the target structure on the initial frame based on user input (clicks



or boxes) prior to any temporal propagation, we first measure segmentation performance on the *prompt-frame* only. We exclude mask-based prompts from this analysis because, by construction, providing the ground-truth first-slice mask yields trivially perfect initialization for both models and therefore does not assess prompt-frame behavior. Table 2 summarizes the DSC across all structures, modalities, and prompt types, with each entry reflecting structure-wise performance aggregated across all datasets in which that structure appears.

Table 2: Prompt-frame DSC (%) for zero-shot segmentation across modalities and anatomical structures using single-click (1,0), multi-click (1,2), and bounding-box prompts. For each pair, the higher DSC is shown in **bold**. Color shading in the table denotes statistical significance for the better model:  $p < 0.001$ ,  $0.001 < p < 0.05$ , and no shading for  $p > 0.05$ .

Modality	Structure	Click (1,0)		Click (1,2)		BBox	
		SAM 2	SAM 3	SAM 2	SAM 3	SAM 2	SAM 3
CT	Adrenal Gland (L)	20.28	<b>25.56</b>	25.81	<b>37.11</b>	77.04	<b>78.38</b>
	Adrenal Gland (R)	9.60	<b>10.65</b>	15.56	<b>20.14</b>	77.45	<b>79.91</b>
	Aorta	60.30	<b>68.14</b>	65.54	<b>69.59</b>	84.05	<b>86.20</b>
	Bladder	10.33	<b>50.53</b>	22.13	<b>59.97</b>	84.49	<b>87.51</b>
	Colon Tumor	25.45	<b>44.05</b>	35.21	<b>52.08</b>	74.76	<b>76.82</b>
	Duodenum	47.65	<b>52.93</b>	52.80	<b>61.04</b>	82.07	<b>85.77</b>
	Esophagus	5.20	<b>33.93</b>	20.68	<b>46.13</b>	85.97	<b>86.85</b>
	Gallbladder	24.38	<b>44.24</b>	37.32	<b>52.06</b>	82.68	<b>84.38</b>
	Inferior Vena Cava	86.25	<b>90.79</b>	84.81	<b>91.24</b>	91.25	<b>93.63</b>
	Kidney (L)	51.79	<b>65.32</b>	60.48	<b>67.76</b>	84.48	<b>87.78</b>
	Kidney (R)	49.94	<b>65.13</b>	61.59	<b>67.24</b>	84.67	<b>88.17</b>
	Liver	30.62	<b>52.88</b>	44.08	<b>57.99</b>	78.42	<b>81.99</b>
	Lung Tumor	5.08	<b>19.21</b>	20.12	<b>29.90</b>	75.89	<b>76.62</b>
	Pancreas	17.96	<b>36.65</b>	28.60	<b>41.79</b>	78.72	<b>81.22</b>
	Pancreas Tumor	22.01	<b>37.43</b>	28.10	<b>42.81</b>	85.55	<b>88.24</b>
	Portal & Splenic Veins	60.85	<b>76.99</b>	66.13	<b>76.82</b>	86.91	<b>88.50</b>
	Prostate	9.06	<b>36.79</b>	25.03	<b>47.22</b>	86.01	<b>87.25</b>
	Spleen	37.91	<b>60.77</b>	54.95	<b>65.60</b>	80.81	<b>85.09</b>
	Stomach	45.89	<b>62.82</b>	56.87	<b>69.60</b>	84.40	<b>87.21</b>
MR	Aorta	29.88	<b>38.59</b>	37.97	<b>40.79</b>	83.66	<b>84.97</b>
	Bladder	13.42	<b>86.99</b>	84.28	<b>87.97</b>	<b>92.42</b>	90.53
	Gallbladder	16.25	<b>26.63</b>	28.62	<b>33.63</b>	82.00	<b>83.32</b>
	Hippocampus (Ant)	6.89	<b>18.70</b>	<b>23.69</b>	20.90	82.12	<b>82.31</b>
	Hippocampus (Post)	3.16	<b>8.92</b>	6.14	<b>13.37</b>	<b>82.82</b>	79.41
	Kidney (L)	41.18	<b>44.71</b>	48.50	<b>49.75</b>	81.88	<b>82.86</b>
	Kidney (R)	40.84	<b>49.34</b>	49.83	<b>52.22</b>	82.26	<b>84.88</b>
	Left Atrium	4.58	<b>9.97</b>	15.16	<b>18.30</b>	75.25	<b>79.67</b>
	Left Ventricle	88.08	<b>95.64</b>	89.10	<b>94.34</b>	96.06	<b>96.75</b>
	Liver	19.82	<b>34.04</b>	29.60	<b>39.75</b>	76.87	<b>78.63</b>
	Myocardium	36.61	<b>79.95</b>	44.74	<b>72.40</b>	53.80	<b>74.25</b>
	Pancreas	4.20	<b>17.38</b>	16.13	<b>23.58</b>	75.27	<b>78.24</b>
	Prostate	13.82	<b>29.82</b>	26.80	<b>35.58</b>	84.08	<b>84.39</b>
	Right Ventricle	73.64	<b>86.55</b>	74.90	<b>89.23</b>	95.07	<b>95.61</b>
	Spleen	20.78	<b>39.74</b>	38.06	<b>49.25</b>	77.78	<b>79.50</b>
US	Carotid Artery (L)	0.38	<b>0.68</b>	<b>3.62</b>	1.61	<b>64.05</b>	57.98
	Carotid Artery (R)	0.18	<b>1.46</b>	<b>14.53</b>	3.30	<b>61.06</b>	60.97
	Jugular Vein (L)	1.14	<b>2.65</b>	<b>6.74</b>	2.93	<b>58.41</b>	55.61
	Jugular Vein (R)	0.40	<b>1.63</b>	<b>6.99</b>	2.50	<b>58.32</b>	54.97
	Left Atrium	17.61	<b>25.31</b>	47.37	<b>60.30</b>	76.99	<b>82.61</b>
	LV Endocardium	31.73	<b>70.46</b>	69.49	<b>73.01</b>	<b>86.77</b>	86.16
	LV Epicardium	23.98	<b>27.65</b>	<b>30.73</b>	26.04	34.15	<b>34.93</b>
Endoscopy	Thyroid	0.99	<b>3.89</b>	<b>5.88</b>	3.70	<b>67.19</b>	65.14
	Abdominal Wall	58.07	<b>72.06</b>	77.34	<b>80.86</b>	<b>87.33</b>	87.24
	Blood	3.06	<b>3.08</b>	42.03	<b>63.01</b>	<b>73.81</b>	72.91
	Connective Tissue	<b>66.34</b>	54.60	<b>68.74</b>	67.61	85.01	<b>88.95</b>
	Cystic Duct	30.50	<b>32.92</b>	<b>29.70</b>	13.45	41.92	<b>48.84</b>
	Fat	62.33	<b>74.23</b>	<b>72.84</b>	62.25	<b>53.74</b>	52.80
	Gallbladder	73.32	<b>83.38</b>	82.24	<b>83.48</b>	88.38	<b>88.44</b>
	GI Tract	53.26	<b>79.72</b>	80.53	<b>86.75</b>	92.02	<b>93.13</b>
	Grasper	81.52	<b>90.12</b>	<b>90.30</b>	88.98	<b>87.00</b>	86.53
	Hepatic Vein	<b>87.78</b>	85.87	<b>88.03</b>	86.91	<b>88.74</b>	87.64
	L-Hook Electrocautery	<b>73.67</b>	72.20	<b>74.06</b>	71.93	89.42	<b>90.96</b>
	Liver	55.80	<b>66.08</b>	63.87	<b>67.55</b>	72.76	<b>73.40</b>
	Liver Ligament	<b>98.38</b>	98.25	<b>98.29</b>	95.66	<b>98.55</b>	98.52

Across the full set of anatomical structures, pathologies, and clinical instruments spanning CT, MRI, ultrasound, and endoscopy, SAM 3 consistently provides markedly stronger prompt initialization than SAM 2. The largest improvements appear for single-click (1,0) prompting, where SAM 3 achieves higher DSC for the vast majority of structures often by wide margins. In CT, these gains are substantial for anatomically small or low-contrast targets such as bladder, pancreas,

esophagus, prostate, and spleen. Improvements are similarly pronounced in MRI, especially for cardiac structures where SAM 3 significantly outperforms SAM 2 for LV, RV, and myocardium under both single- and multi-click prompting.

Multi-click prompting (1,2) reduces ambiguity for both models, yet SAM 3 retains a clear advantage in nearly all CT and MRI structures with statistically significant gains, frequently with  $p < 0.001$ .

For bounding-box prompts, where the spatial support is considerably less ambiguous, the performance gap narrows but does not disappear. SAM 3 continues to produce higher DSC for most CT and MRI structures, although with smaller margins. We also see some instances of SAM 2 performing slightly better than SAM 3 (e.g., MR Bladder and MR Hippocampus Posterior). Box prompts achieve the highest absolute accuracy for both models, and here the differences between the two models typically fall within a modest range ( $\sim 5$  DSC points) with the exception of MR Myocardium where SAM 3 beats SAM 2 by about 20 DSC points. This indicates that when coarse spatial localization is supplied explicitly, SAM 3 still provides a slightly stronger prompt-image response, but its relative advantage is less dominant.

Ultrasound exhibits a mixed pattern. For segmentation of cardiac chambers in cine sequences (LA, LV endocardium, LV epicardium), SAM 3 achieves substantially higher DSC for click prompts, reflecting improved localization. In contrast, for the SegThy dataset (thyroid, carotid arteries, and jugular veins), both models exhibit near-total failure under click prompting, with DSCs frequently remaining in the single digits. Segmentation accuracy becomes meaningful only when bounding-box prompts are supplied; in this viable regime, SAM 2 consistently outperforms SAM 3 across the thyroid and all vascular targets.

For endoscopy (CholecSeg8K), SAM 3 shows an advantage under single-click (1,0) prompting, outperforming SAM 2 for the majority of the tissue and instrument classes. However, under multi-click (1,2) and bounding-box prompts, the results are more balanced: SAM 2 and SAM 3 each achieve higher DSC for different categories, and no model dominates across all structures. Notably, even when numerical differences are large between the two models, none of these comparisons reach statistical significance because CholecSeg8K contains only a small number of annotated videos, which limits the power of paired significance testing. Overall, SAM 3 provides a stronger initialization when the prompt signal is sparse, while both models perform comparably when additional spatial guidance is provided.

Overall, prompt-frame evaluation shows that across modalities, SAM 3 typically offers an advantage over SAM 2 in interpreting both sparse and coarse spatial prompts. These effects are strongest for single-click prompts, remain significant for multi-click prompts, and persist, though with smaller magnitude, for bounding-box prompting.

### 3.2 Full-Volume/Sequence Segmentation Accuracy

While prompt-frame accuracy captures initialization quality, clinical applications require accurate segmentation across full 3D volumes or complete temporal sequences. Full-volume accuracy, therefore, reflects the combined effect of both initialization and propagation under SAM 2’s memory-based architecture and SAM 3’s redesigned tracking pathway. Full-volume DSC under all prompting regimes are reported in Table 3, where each entry reflects structure-wise performance aggregated across all datasets in which that structure appears. To complement these aggregated results and highlight dataset-specific behavior, Figures 2 and 3 present per-dataset boxplots for all CT, MRI, ultrasound, and endoscopy datasets.

Across CT datasets, SAM 3 achieves higher DSC than SAM 2 under single-click and multi-click prompting for most organs, although the gains are smaller than in the prompt-frame setting, indicating that some of the initialization advantage is attenuated during propagation. Under bounding-box prompting, the gap narrows further. Moreover for bounding box, while SAM 3 remains ahead for many large abdominal organs, SAM 2 achieves higher full-volume DSC for several structures including spleen, kidneys, and gallbladder, indicating that its propagation can be more stable when sufficient spatial guidance is provided. Under mask prompting, where we have a perfect initialization, SAM 2 often performs comparably to or slightly better than SAM 3, showing that SAM 2’s propagation remains competitive once prompt ambiguity is reduced.

In MRI, SAM 3 shows clear improvements under single-click prompting for many structures, particularly cardiac regions such as LV, RV, and myocardium. However, several abdominal organs

Table 3: Full-volume/sequence DSC (%) for zero-shot segmentation across modalities and anatomical structures using single-click (1,0), multi-click (1,2), bounding-box, and mask prompts. For each pair, the higher DSC is shown in **bold**. Color shading in the table denotes statistical significance for the better model:  $p < 0.001$ ,  $0.001 < p < 0.05$ , and no shading for  $p > 0.05$ .

Modality	Structure	Click (1,0)		Click (1,2)		BBox		Mask	
		SAM 2	SAM 3	SAM 2	SAM 3	SAM 2	SAM 3	SAM 2	SAM 3
CT	Adrenal Gland (L)	19.13	<b>25.14</b>	20.79	<b>34.54</b>	<b>49.02</b>	46.67	<b>47.59</b>	41.78
	Adrenal Gland (R)	8.93	<b>11.28</b>	10.18	<b>19.86</b>	<b>45.52</b>	44.86	<b>44.41</b>	39.53
	Aorta	68.71	<b>78.72</b>	72.07	<b>81.17</b>	68.41	<b>74.58</b>	67.22	<b>73.42</b>
	Bladder	3.63	<b>10.32</b>	6.56	<b>10.93</b>	10.60	<b>12.03</b>	9.72	<b>11.61</b>
	Colon Tumor	11.16	<b>15.98</b>	13.03	<b>17.27</b>	16.58	<b>18.24</b>	18.53	<b>19.36</b>
	Duodenum	25.68	<b>30.68</b>	26.92	<b>32.36</b>	31.34	<b>33.23</b>	32.78	<b>34.35</b>
	Esophagus	3.88	<b>37.00</b>	8.12	<b>48.28</b>	60.60	<b>68.44</b>	59.75	<b>68.22</b>
	Gallbladder	22.88	<b>30.39</b>	31.68	<b>34.53</b>	<b>49.62</b>	38.00	<b>48.47</b>	36.68
	Inferior Vena Cava	70.08	<b>79.28</b>	65.21	<b>78.77</b>	69.89	<b>78.54</b>	70.41	<b>78.47</b>
	Kidney (L)	58.72	<b>59.35</b>	<b>66.18</b>	61.38	<b>75.75</b>	64.70	<b>76.67</b>	64.43
	Kidney (R)	54.02	<b>65.66</b>	66.01	<b>67.43</b>	<b>78.15</b>	72.52	<b>78.78</b>	72.32
	Liver	44.18	<b>65.85</b>	52.10	<b>71.53</b>	67.72	<b>74.94</b>	67.21	<b>74.99</b>
	Lung Tumor	6.78	<b>18.72</b>	13.95	<b>30.06</b>	<b>44.22</b>	42.48	<b>46.33</b>	43.20
	Pancreas	19.24	<b>32.71</b>	23.93	<b>34.87</b>	28.00	<b>33.93</b>	27.38	<b>33.73</b>
	Pancreas Tumor	11.64	<b>17.00</b>	13.32	<b>18.72</b>	27.09	<b>28.47</b>	26.49	<b>29.06</b>
	Portal & Splenic Veins	27.70	<b>31.44</b>	31.00	<b>31.63</b>	<b>36.55</b>	34.05	<b>34.69</b>	34.33
	Prostate	2.56	<b>7.24</b>	5.32	<b>7.58</b>	<b>11.88</b>	8.70	<b>9.26</b>	8.75
	Spleen	46.20	<b>57.13</b>	56.51	<b>59.77</b>	<b>74.25</b>	63.03	<b>74.96</b>	62.56
	Stomach	36.80	<b>50.34</b>	45.73	<b>52.07</b>	49.43	<b>53.84</b>	49.42	<b>55.86</b>
MR	Aorta	42.58	<b>58.67</b>	46.05	<b>63.01</b>	40.83	<b>58.59</b>	42.12	<b>58.30</b>
	Bladder	0.48	<b>7.49</b>	<b>55.49</b>	6.80	<b>76.91</b>	7.29	<b>47.90</b>	6.34
	Gallbladder	17.92	<b>19.03</b>	<b>26.15</b>	25.06	<b>44.60</b>	30.19	<b>43.74</b>	30.57
	Hippocampus (Ant)	12.19	<b>16.96</b>	11.16	<b>17.86</b>	22.16	<b>23.62</b>	24.86	<b>25.37</b>
	Hippocampus (Post)	12.94	<b>33.89</b>	14.00	<b>33.10</b>	16.91	<b>18.43</b>	<b>23.74</b>	23.46
	Kidney (L)	<b>45.19</b>	44.44	<b>51.67</b>	48.77	<b>58.07</b>	49.23	<b>56.81</b>	48.07
	Kidney (R)	52.73	<b>54.43</b>	<b>60.53</b>	55.93	<b>63.28</b>	58.29	<b>64.40</b>	57.42
	Left Atrium	17.72	<b>30.41</b>	26.22	<b>43.65</b>	22.47	<b>44.23</b>	18.94	<b>39.46</b>
	Left Ventricle	80.38	<b>93.17</b>	74.32	<b>92.54</b>	88.21	<b>93.62</b>	89.88	<b>94.21</b>
	Liver	36.37	<b>57.46</b>	42.94	<b>63.12</b>	51.25	<b>56.39</b>	48.65	<b>56.42</b>
	Myocardium	36.92	<b>78.24</b>	39.56	<b>74.10</b>	52.95	<b>72.88</b>	82.46	<b>84.75</b>
	Pancreas	6.49	<b>22.87</b>	11.26	<b>24.57</b>	18.24	<b>24.35</b>	17.72	<b>23.83</b>
	Prostate	12.22	<b>17.70</b>	15.90	<b>19.59</b>	<b>28.12</b>	23.61	<b>28.10</b>	23.65
	Right Ventricle	52.39	<b>77.29</b>	46.01	<b>82.76</b>	80.41	<b>85.60</b>	82.61	<b>86.37</b>
	Spleen	26.91	<b>49.94</b>	36.22	<b>56.99</b>	56.52	<b>58.78</b>	<b>59.15</b>	59.11
US	Carotid Artery (L)	<b>13.55</b>	10.99	<b>23.53</b>	23.46	5.98	<b>56.65</b>	5.65	<b>41.36</b>
	Carotid Artery (R)	1.14	<b>11.92</b>	17.83	<b>21.67</b>	17.00	<b>51.12</b>	22.86	<b>60.69</b>
	Jugular Vein (L)	7.76	<b>30.69</b>	19.62	<b>30.55</b>	5.45	<b>35.30</b>	5.57	<b>39.52</b>
	Jugular Vein (R)	2.33	<b>17.84</b>	7.93	<b>31.92</b>	10.71	<b>28.16</b>	21.49	<b>29.05</b>
	Left Atrium	19.49	<b>28.59</b>	30.34	<b>66.11</b>	79.08	<b>83.82</b>	90.34	<b>90.60</b>
	LV Endocardium	27.47	<b>67.48</b>	62.50	<b>72.98</b>	85.38	<b>85.79</b>	<b>91.93</b>	91.19
	LV Epicardium	24.15	<b>28.04</b>	25.84	<b>27.24</b>	41.54	<b>42.29</b>	<b>82.20</b>	78.17
	Thyroid	10.13	<b>32.65</b>	19.87	<b>53.90</b>	10.53	<b>28.10</b>	7.27	<b>27.58</b>
Endoscopy	Abdominal Wall	55.77	<b>67.42</b>	58.14	<b>79.41</b>	69.20	<b>82.56</b>	81.23	<b>87.81</b>
	Blood	5.11	<b>12.94</b>	7.91	<b>38.80</b>	25.77	<b>33.39</b>	10.14	<b>38.22</b>
	Connective Tissue	<b>70.45</b>	66.32	<b>65.73</b>	61.16	61.14	<b>72.24</b>	69.91	<b>74.55</b>
	Cystic Duct	<b>0.15</b>	0.14	<b>0.20</b>	0.14	<b>1.42</b>	0.20	<b>0.16</b>	0.16
	Fat	60.00	<b>71.43</b>	<b>61.71</b>	60.90	38.42	<b>40.78</b>	87.20	<b>88.14</b>
	Gallbladder	72.49	<b>79.18</b>	74.95	<b>75.38</b>	<b>82.81</b>	81.17	78.73	<b>83.80</b>
	GI Tract	37.83	<b>65.02</b>	31.49	<b>70.83</b>	69.57	<b>75.84</b>	<b>76.77</b>	73.30
	Grasper	74.59	<b>82.47</b>	75.64	<b>78.21</b>	77.65	<b>78.93</b>	76.35	<b>80.76</b>
	Hepatic Vein	19.49	<b>21.62</b>	20.05	<b>21.70</b>	20.71	<b>21.64</b>	20.76	<b>23.08</b>
	L-Hook Electrocautery	<b>66.84</b>	64.50	65.91	<b>68.58</b>	65.91	<b>69.64</b>	66.78	<b>69.98</b>
	Liver	57.40	<b>59.78</b>	60.89	<b>68.48</b>	<b>67.76</b>	67.12	88.49	<b>90.33</b>
	Liver Ligament	<b>98.69</b>	98.29	<b>98.65</b>	96.16	<b>98.76</b>	98.55	<b>98.72</b>	98.51

including gallbladder and both kidneys show much closer DSC values between the two models. Under multi-click prompting, these same structures begin to favor SAM 2, reflecting that additional spatial cues reduce the relative benefit of SAM 3’s prompt interpretation. This trend becomes more pronounced under bounding-box and mask prompts, where SAM 2 frequently achieves higher full-volume accuracy for gallbladder, kidneys, prostate, and bladder. Notably, the MR Bladder highlights this distinct failure mode: while SAM 3 achieved high accuracy in the prompt-frame (Table 2), its full-volume performance collapses to near-zero (7.29%), indicating a catastrophic failure to track the structure despite successful initialization. In contrast, SAM 2 maintains robust propagation (76.91%), demonstrating superior temporal stability for this structure.

Ultrasound exhibits modality-specific differences. In CAMUS cardiac cine sequences, SAM 3 achieves higher accuracy under both single-click and multi-click prompting, and generally maintains a small advantage under bounding boxes. Under mask prompting, however, performance becomes

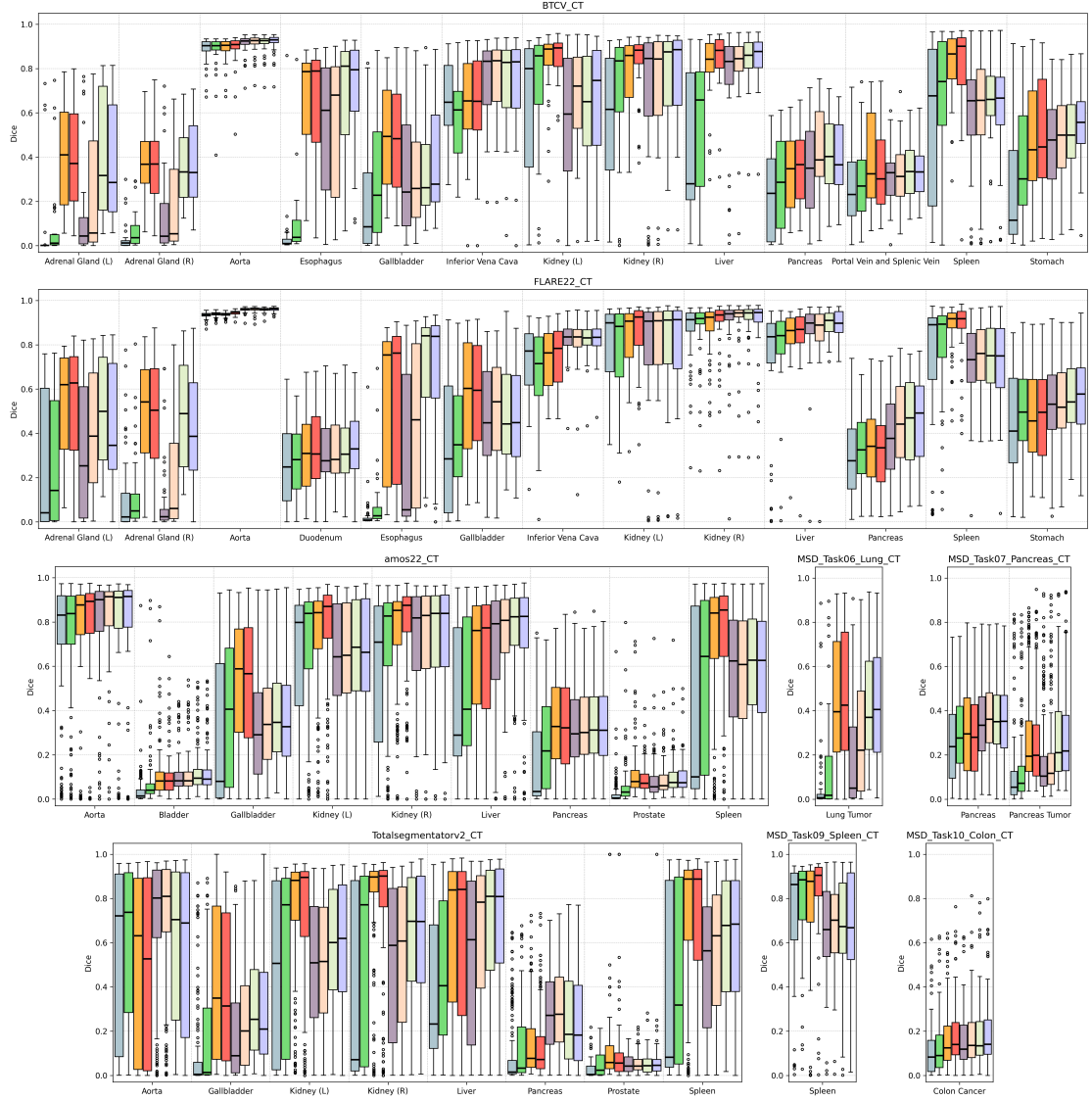


Fig. 2: Boxplots showing zero-shot segmentation performance for all anatomical structures in each CT dataset. For every structure, eight boxplots appear in a fixed left-to-right order corresponding to the four prompting modes of SAM 2 followed by the four prompting modes of SAM 3 [SAM 2 (1,0), SAM 2 (1,2), SAM 2 (BBox), SAM 2 (Mask), SAM 3 (1,0), SAM 3 (1,2), SAM 3 (BBox), SAM 3 (Mask)].

comparable and shifts toward SAM 2 for LV endocardium and epicardium. In SegThy 3D ultrasound, there is a striking inversion of behavior between initialization and propagation. While prompt-frame analysis (Table 2) showed that SAM 2 provided superior initialization for carotid and jugular vessels for bounding box prompts, Table 3 reveals that SAM 2 fails catastrophically during propagation for these targets, with DSCs dropping to single digits (e.g., Left Carotid: 5.98%). In contrast, SAM 3 successfully maintains its initialization throughout the volume (56.65%).

Endoscopy (CholecSeg8K) follows a similar trajectory: SAM 3 achieves higher DSC under single-click prompting for most tissue and instrument categories, but the gap diminishes with multi-click and bounding-box prompts, and few structures start favoring SAM 2. Despite some large numerical differences in individual structures, none of the comparisons achieve statistical significance due to the small number of annotated videos, which limits the power of paired testing. When mask prompts are used, both models show similar performance across most structures.

To illustrate the characteristic behaviors underlying these quantitative differences, Figure 4 presents representative cases where SAM 3 outperforms SAM 2 due to stronger initial localization under sparse prompts. Conversely, Figure 5 shows examples where SAM 2 achieves more stable

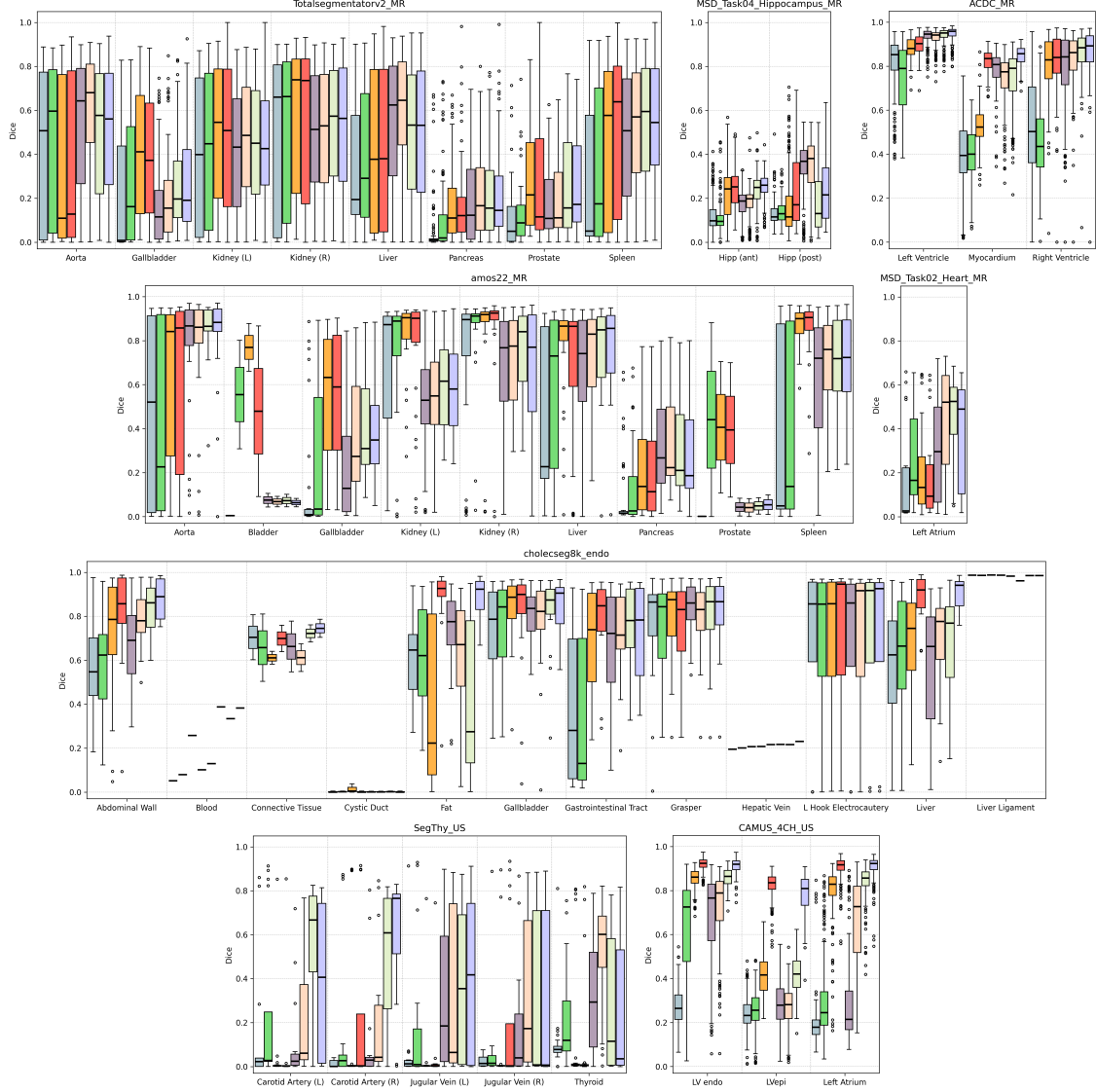


Fig. 3: Boxplots showing zero-shot segmentation performance for all anatomical structures in each MR, US, and Endoscopy dataset. For every structure, eight boxplots appear in a fixed left-to-right order corresponding to the four prompting modes of SAM 2 followed by the four prompting modes of SAM 3 [SAM 2 (1,0), SAM 2 (1,2), SAM 2 (BBox), SAM 2 (Mask), SAM 3 (1,0), SAM 3 (1,2), SAM 3 (BBox), SAM 3 (Mask)].

slice-to-slice or frame-to-frame propagation, leading to higher full-volume accuracy despite similar or stronger initialization.

### 3.3 Performance Behavior as a Function of Prompt Strength

Across all modalities, both models show predictable yet distinct trajectories as prompt strength increases from single-click to multi-click, bounding-box, and mask prompts. We categorize the performance behavior into following two distinct regimes: (1) sparse guidance (clicks), where the model must infer the object from sparse prompts before propagating, and (2) strong spatial guidance (bounding boxes and masks), where the model must primarily track a defined region.

**Sparse Guidance (Clicks).** When prompts are limited to clicks, SAM 3 exhibits a dominant advantage. Its unified perception encoder allows it to infer semantic structure from minimal input, achieving significantly higher DSCs than SAM 2 across the vast majority of anatomical targets in CT, MRI, and Endoscopy. SAM 2 frequently struggles in this regime, often failing to localize the



target entirely (as seen in all three examples of Figure 4) or producing under-segmented masks that degrade further during propagation.

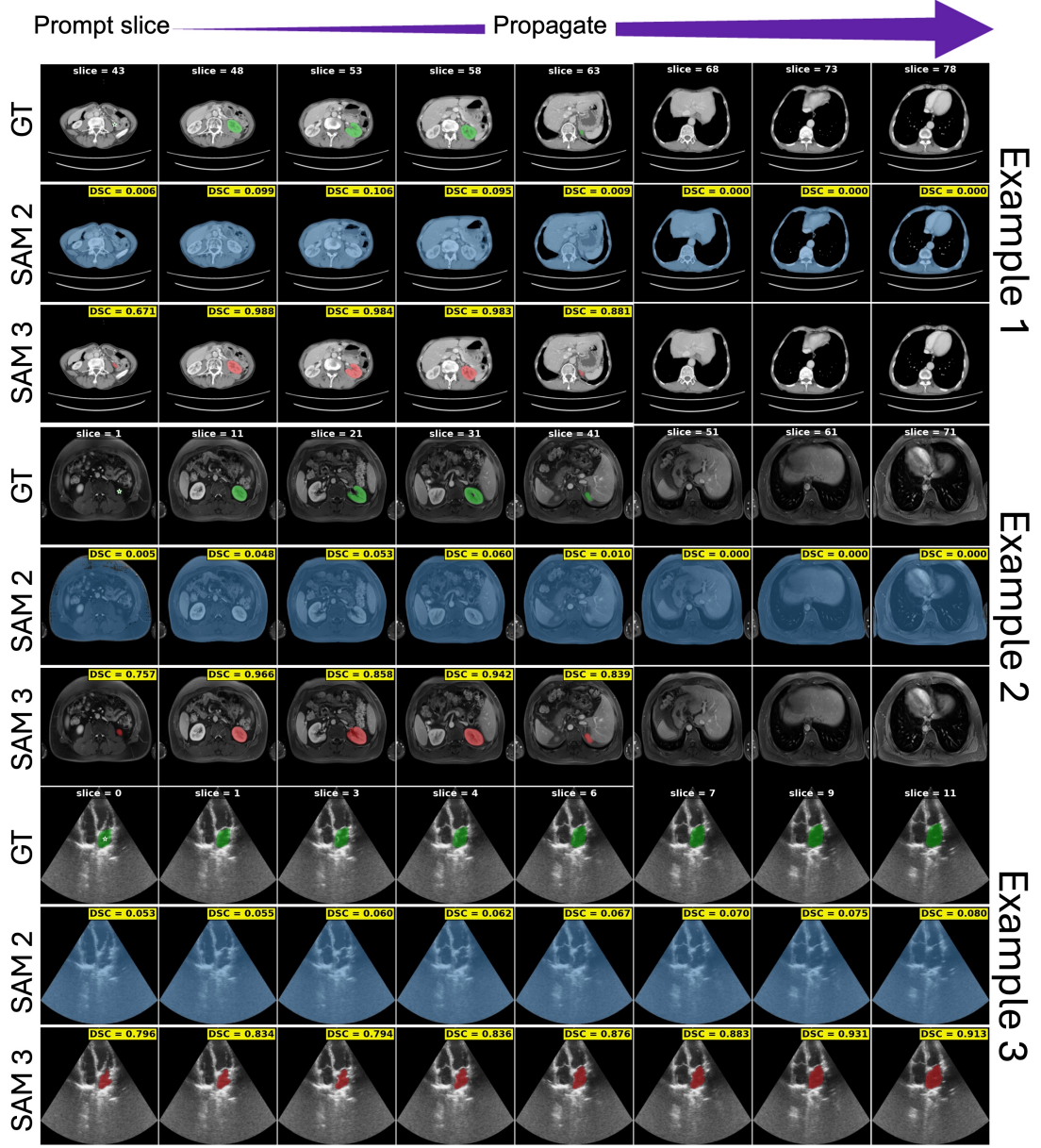


Fig. 4: Qualitative examples illustrating cases where SAM 3 outperforms SAM 2. All three examples are for single-click (1,0) prompting and show SAM 3’s superior prompt initialization by better localizing the structure even under sparse prompts. SAM 3 produces accurate, spatially coherent segmentations even for small or low-contrast structures, whereas SAM 2 exhibits failure to localize the target on the prompted frame, resulting in over-segmentation and notably lower DSC. [Colors: ground truth in green, SAM 2 predictions in blue, and SAM 3 predictions in red.]

**Strong Spatial Guidance (Bounding box and Mask).** As prompts become more informative i.e., either coarse localization (boxes) or exact boundaries (masks) are available, the performance gap does not simply close; rather, the two models diverge into distinct areas of specialization. The global dominance of SAM 3 disappears, replaced by a structural dichotomy:

- **SAM 2.** For anatomically distinct, encapsulated, and compact organs, such as the spleen, kidneys, bladder, and prostate, SAM 2 frequently matches or outperforms SAM 3 once a bounding box or mask is provided. This trend is consistent across CT and MRI, suggesting



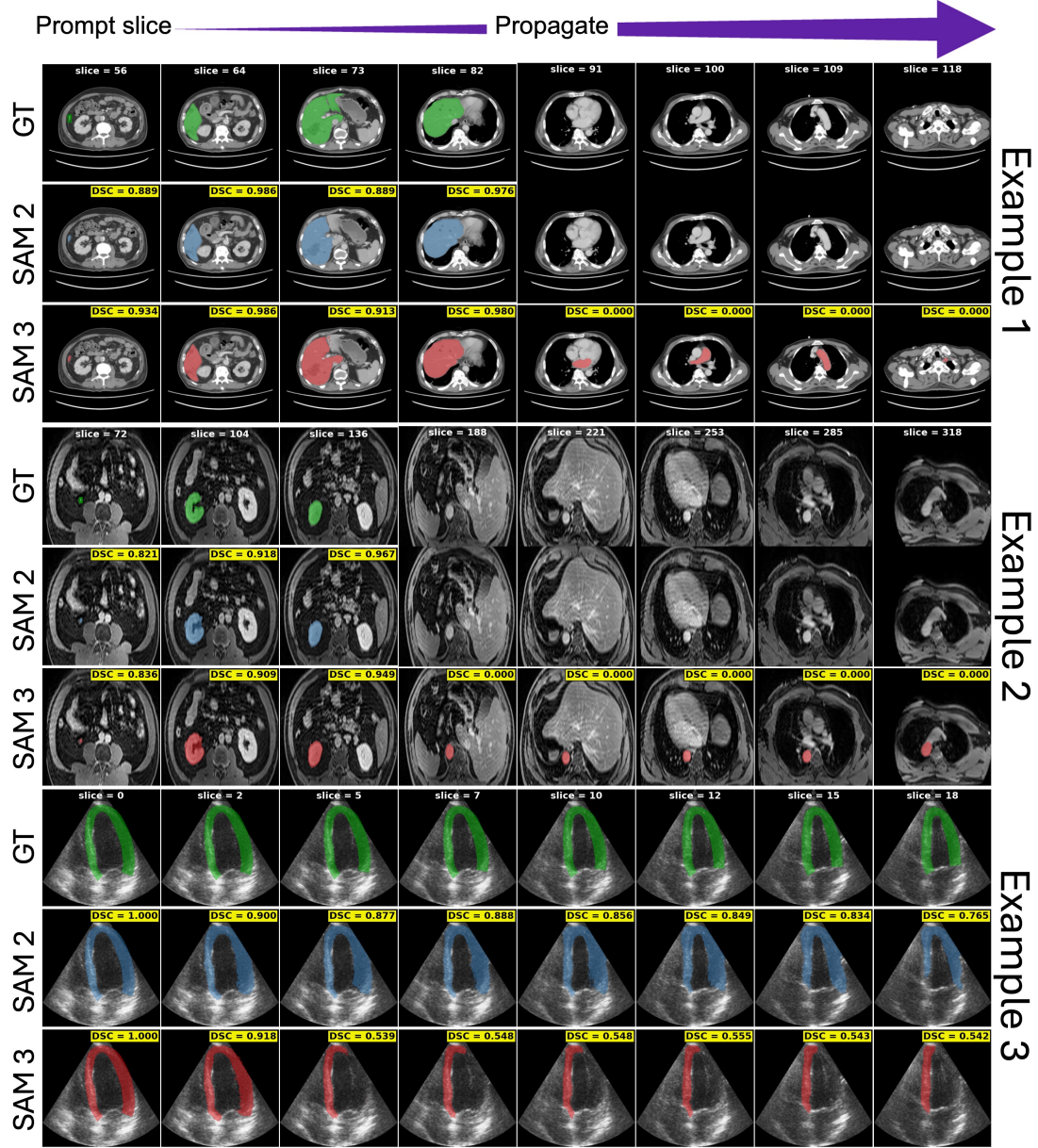


Fig. 5: Qualitative examples illustrating cases where SAM 2 outperforms SAM 3. Examples 1–2 are for bbox and example 3 is for mask prompt. In these examples, SAM 3 provides strong initial localization but exhibits propagation failures, including hallucinated residual masks in later slices (Examples 1–2) and erosion or collapse of structure boundaries under low contrast or motion (Example 3). In contrast, SAM 2 maintains more stable slice-to-slice consistency and suppresses spurious predictions, yielding higher DSC. [Colors: ground truth in green, SAM 2 predictions in blue, and SAM 3 predictions in red.]

that SAM 2’s memory-based architecture is highly robust at maintaining the boundaries of rigid or semi-rigid objects against frame-to-frame background noise.

- **SAM 3.** Conversely, for elongated, thin, or poorly contrasted structures, such as vessels (Aorta, IVC, Carotids), gastrointestinal tracts, and soft tissues (Pancreas, Liver, Thyroid), SAM 3 retains a significant advantage. Even with perfect mask initialization, SAM 2 often struggles to propagate these targets, exhibiting drift or collapse (e.g., SegThy carotid arteries dropping to  $< 6\%$  DSC). SAM 3’s tracker demonstrates superior robustness for these complex topologies.

In summary, increasing prompt strength neutralizes SAM 3’s initialization advantage but exposes SAM 2’s propagation limitations on complex anatomy. While SAM 2 becomes the safer

choice for "standard" abdominal organs, SAM 3 remains the necessary choice for vascular and soft-tissue targets.

### 3.4 Overall Interpretation and Summary of Findings

Taken together, the prompt-frame and full-volume evaluations show that SAM 2 and SAM 3 exhibit complementary strengths rather than a single performance hierarchy. Their differences arise from a trade-off between prompt interpretation (understanding what to segment) and frame-to-frame consistency (remembering what was segmented). We summarize our findings as follows:

- **Initialization advantages for SAM 3.** When prompts are limited to clicks, SAM 3 exhibits a dominant advantage. Its unified perception encoder allows it to infer semantic structure from minimal input, achieving significantly higher DSCs than SAM 2 across the vast majority of anatomical targets in CT, MRI, and Endoscopy.
- **Propagation Trade-off (Compact vs. Complex).** Once the target is initialized (via bounding box or mask), propagation behavior splits by anatomical type. From our experiments, we see that SAM 2 demonstrates superior stability for compact organs (Kidney, Spleen, Bladder), often showing less "forgetting" across a volume than SAM 3. However, SAM 3 demonstrates superior tracking for complex, continuous, or vascular structures, where SAM 2 frequently fails to maintain the segmentation despite better initialization.
- **The "Unreliable Propagator" Risk.** A critical finding is that high initialization accuracy does not guarantee propagation success. This is most evident in the MRI Bladder and US SegThy datasets, where models (SAM 3 in MRI, SAM 2 in US) achieve excellent prompt-frame scores but suffer catastrophic collapse during the sequence.

Overall, for interactive tasks (clicks), SAM 3 is the clear recommendation due to its superior prompt interpretation. When more careful prompts are present (bounding boxes/masks), the choice depends on the anatomy: SAM 2 can be used for compact organs to maximize stability, and SAM 3 can be used for vessels and irregular soft tissues to prevent tracking failure. For practical medical segmentation workflows, the optimal model depends on the balance between initialization difficulty and propagation demands within a given modality and task.

## 4 Conclusion

This study presents the first large-scale, systematic comparison of SAM 2 and SAM 3 for zero-shot segmentation of 3D medical data under controlled prompting conditions. By evaluating single-click, multi-click, bounding-box, and mask-based initialization across sixteen datasets and 54 anatomical structures, we disentangle the contributions of prompt interpretation and propagation behavior in both models.

Across all modalities, SAM 3 provides markedly stronger prompt interpretation. It consistently produces superior prompt-frame accuracy for both sparse and moderately informative prompts, effectively solving the initialization bottleneck that frequently hampers interactive segmentation. These advantages extend to full-volume performance for the majority of clinical targets, including vascular networks, gastrointestinal structures, and soft tissues in ultrasound and endoscopy. In contrast, while SAM 2 remains a highly effective propagator for compact, well-defined organs (e.g., spleen, kidneys) once sufficient spatial support is provided, it lacks the versatility of SAM 3, often exhibiting propagation failure on complex or low-contrast anatomy even when initialized with perfect masks.

Overall, the results position SAM 3 as the stronger and more robust foundation model for medical imaging. Its architectural improvements in prompt interpretation and tracking allow it to handle a wider diversity of anatomical shapes and modalities than its predecessor. While SAM 2 remains a valid choice for pipelines specifically targeting rigid abdominal organs using bounding box or mask prompts, SAM 3 offers the necessary generalization capabilities for broad-spectrum clinical applications. These findings support the adoption of SAM 3 as the new baseline for zero-shot medical segmentation and suggest that future efforts should focus on leveraging its semantic capabilities to further enhance automation.

One limitation of this study is that we restrict our analysis to visual prompts, a deliberate choice made to perform a backwards compatibility check and evaluate whether SAM 3 can directly replace SAM 2 in 3D medical annotation workflows without requiring concept prompts or language-based reasoning. As a consequence, we do not examine the concept- and text-based mechanisms that SAM 3 introduced for open-vocabulary and semantic 3D segmentation. This direction is attracting growing attention, and recent work such as Voxel [21] further illustrates the community’s interest in applying vision–language models to open-vocabulary and concept-driven segmentation of medical data. Extending our framework to incorporate these semantic prompting capabilities, and assessing SAM 3 with its language and concept modules enabled, will be an important direction for future investigation.

## References

1. A. Kirillov, E. Mintun, N. Ravi, H. Mao, C. Rolland, L. Gustafson, T. Xiao, S. Whitehead, A. C. Berg, W.-Y. Lo *et al.*, “Segment anything,” in *Proceedings of the IEEE/CVF International Conference on Computer Vision*, 2023, pp. 4015–4026.
2. N. Ravi, V. Gabeur, Y.-T. Hu, R. Hu, C. Ryali, T. Ma, H. Khedr, R. Rädle, C. Rolland, L. Gustafson *et al.*, “Sam 2: Segment anything in images and videos,” *arXiv preprint arXiv:2408.00714*, 2024.
3. N. Carion, L. Gustafson, Y.-T. Hu, S. Debnath, R. Hu, D. Suris, C. Ryali, K. V. Alwala, H. Khedr, A. Huang, J. Lei, T. Ma, B. Guo, A. Kalla, M. Marks, J. Greer, M. Wang, P. Sun, R. Rädle, T. Afouras, E. Mavroudi, K. Xu, T.-H. Wu, Y. Zhou, L. Momeni, R. Hazra, S. Ding, S. Vaze, F. Porcher, F. Li, S. Li, A. Kamath, H. K. Cheng, P. Dollár, N. Ravi, K. Saenko, P. Zhang, and C. Feichtenhofer, “Sam 3: Segment anything with concepts,” 2025. [Online]. Available: <https://arxiv.org/abs/2511.16719>
4. N. Carion, F. Massa, G. Synnaeve, N. Usunier, A. Kirillov, and S. Zagoruyko, “End-to-end object detection with transformers,” in *European conference on computer vision*. Springer, 2020, pp. 213–229.
5. S. Sengupta, S. Chakrabarty, and R. Soni, “Is sam 2 better than sam in medical image segmentation?” in *Medical Imaging 2025: Image Processing*, vol. 13406. SPIE, 2025, pp. 666–672.
6. H. Dong, H. Gu, Y. Chen, J. Yang, Y. Chen, and M. A. Mazurowski, “Segment anything model 2: an application to 2d and 3d medical images,” *arXiv preprint arXiv:2408.00756*, 2024.
7. J. Ma, S. Kim, F. Li, M. Baharoon, R. Asakereh, H. Lyu, and B. Wang, “Segment anything in medical images and videos: Benchmark and deployment,” *arXiv preprint arXiv:2408.03322*, 2024.
8. C. Ryali, Y.-T. Hu, D. Bolya, C. Wei, H. Fan, P.-Y. Huang, V. Aggarwal, A. Chowdhury, O. Pour-saeed, J. Hoffman *et al.*, “Hiera: A hierarchical vision transformer without the bells-and-whistles,” in *International conference on machine learning*. PMLR, 2023, pp. 29 441–29 454.
9. Y. Ji, H. Bai, C. Ge, J. Yang, Y. Zhu, R. Zhang, Z. Li, L. Zhanng, W. Ma, X. Wan *et al.*, “Amos: A large-scale abdominal multi-organ benchmark for versatile medical image segmentation,” *Advances in neural information processing systems*, vol. 35, pp. 36 722–36 732, 2022.
10. B. Landman, Z. Xu, J. Igelsias, M. Styner, T. Langerak, and A. Klein, “Miccai multi-atlas labeling beyond the cranial vault—workshop and challenge,” in *Proc. MICCAI multi-atlas labeling beyond cranial vault—workshop challenge*, vol. 5. Munich, Germany, 2015, p. 12.
11. J. Ma, Y. Zhang, S. Gu, C. Ge, S. Mae, A. Young, C. Zhu, X. Yang, K. Meng, Z. Huang *et al.*, “Unleashing the strengths of unlabelled data in deep learning-assisted pan-cancer abdominal organ quantification: the flare22 challenge,” *The Lancet Digital Health*, vol. 6, no. 11, pp. e815–e826, 2024.
12. M. Antonelli, A. Reinke, S. Bakas, K. Farahani, A. Kopp-Schneider, B. A. Landman, G. Litjens, B. Menze, O. Ronneberger, R. M. Summers *et al.*, “The medical segmentation decathlon,” *Nature communications*, vol. 13, no. 1, p. 4128, 2022.
13. A. L. Simpson, M. Antonelli, S. Bakas, M. Bilello, K. Farahani, B. Van Ginneken, A. Kopp-Schneider, B. A. Landman, G. Litjens, B. Menze *et al.*, “A large annotated medical image dataset for the development and evaluation of segmentation algorithms,” *arXiv preprint arXiv:1902.09063*, 2019.
14. J. Wasserthal, H.-C. Breit, M. T. Meyer, M. Pradella, D. Hinck, A. W. Sauter, T. Heye, D. T. Boll, J. Cyriac, S. Yang *et al.*, “Totalsegmentator: robust segmentation of 104 anatomic structures in ct images,” *Radiology: Artificial Intelligence*, vol. 5, no. 5, 2023.
15. O. Bernard, A. Lalande, C. Zotti, F. Cervenansky, X. Yang, P.-A. Heng, I. Cetin, K. Lekadir, O. Camara, M. A. G. Ballester *et al.*, “Deep learning techniques for automatic mri cardiac multi-structures segmentation and diagnosis: is the problem solved?” *IEEE transactions on medical imaging*, vol. 37, no. 11, pp. 2514–2525, 2018.
16. T. A. D’Antonoli, L. K. Berger, A. K. Indrakanti, N. Vishwanathan, J. Weiß, M. Jung, Z. Berkarda, A. Rau, M. Reiser, T. Küstner *et al.*, “Totalsegmentator mri: Sequence-independent segmentation of 59 anatomical structures in mr images,” *arXiv preprint arXiv:2405.19492*, 2024.
17. S. Leclerc *et al.*, “Deep learning for segmentation using an open large-scale dataset in 2d echocardiography,” *IEEE transactions on medical imaging*, vol. 38, no. 9, pp. 2198–2210, 2019.

18. M. Krönke, C. Eilers, D. Dimova, M. Köhler, G. Buschner, L. Schweiger, L. Konstantinidou, M. Makowski, J. Nagarajah, N. Navab *et al.*, “Tracked 3d ultrasound and deep neural network-based thyroid segmentation reduce interobserver variability in thyroid volumetry,” *Plos one*, vol. 17, no. 7, p. e0268550, 2022.
19. W.-Y. Hong, C.-L. Kao, Y.-H. Kuo, J.-R. Wang, W.-L. Chang, and C.-S. Shih, “Cholecseg8k: a semantic segmentation dataset for laparoscopic cholecystectomy based on cholec80,” *arXiv preprint arXiv:2012.12453*, 2020.
20. A. P. Twinanda, S. Shehata, D. Mutter, J. Marescaux, M. De Mathelin, and N. Padoy, “Endonet: a deep architecture for recognition tasks on laparoscopic videos,” *IEEE transactions on medical imaging*, vol. 36, no. 1, pp. 86–97, 2016.
21. M. Rokuss, M. Langenberg, Y. Kirchhoff, F. Isensee, B. Hamm, C. Ulrich, S. Regnery, L. Bauer, E. Katsigiannopulos, T. Norajitra *et al.*, “Voxtell: Free-text promptable universal 3d medical image segmentation,” *arXiv preprint arXiv:2511.11450*, 2025.